# Crimson Behemoth: A massive clumpy structure hosting a dusty AGN at z=4.91

Takumi S. Tanaka, John D. Silverman, Yurina Nakazato, Masafusa Onoue, Kazuhiro Shimasaku, Yoshinobu Fudamoto, Seiji Fujimoto, Xuheng Ding, Andreas L. Faisst, Francesco Valentino, et al.

*Publications of the Astronomical Society of Japan*, 2024, **76**(6), 1323–1335
https://doi.org/10.1093/pasj/psae091
Advance access publication date: 2024 November 4

# Crimson Behemoth: A massive clumpy structure hosting a dusty AGN at $z = 4.91$

**Takumi S. Tanaka**[1,2,3,*] **John D. Silverman**[1,2,3,4] **Yurina Nakazato**[5] **Masafusa Onoue**[2,6] **Kazuhiro Shimasaku**[1,7] **Yoshinobu Fudamoto**[8] **Seiji Fujimoto**[9,10] **Xuheng Ding**[11] **Andreas L. Faisst**[12] **Francesco Valentino**[10,13] **Shuowen Jin**[10,14] **Christopher C. Hayward**[15] **Vasily Kokorev**[9,16] **Daniel Ceverino**[17,18] **Boris S. Kalita**[2,3,6] **Caitlin M. Casey**[9,10] **Zhaoxuan Liu**[1,2,3] **Aidan Kaminsky**[19] **Qinyue Fei**[20] **Irham T. Andika**[21,22] **Erini Lambrides**[23] **Hollis B. Akins**[9] **Jeyhan S. Kartaltepe**[24] **Anton M. Koekemoer**[25] **Henry Joy McCracken**[26] **Jason Rhodes**[27] **Brant E. Robertson**[28] **Maximilien Franco**[9] **Daizhong Liu**[29] **Nima Chartab**[30] **Steven Gillman**[10,14] **Ghassem Gozaliasl**[31,32] **Michaela Hirschmann**[33,34] **Marc Huertas-Company**[35,36,37,38,39] **Richard Massey**[40] **Namrata Roy**[4] **Zahra Sattari**[30,41] **Marko Shuntov**[26] **Joseph Sterling**[19] **Sune Toft**[10,42] **Benny Trakhtenbrot**[43] **Naoki Yoshida**[2,5,7] **and Jorge A. Zavala**[44]

[1] Department of Astronomy, Graduate School of Science, The University of Tokyo, 7-3-1 Hongo, Bunkyo-ku, Tokyo 113-0033, Japan
[2] Kavli Institute for the Physics and Mathematics of the Universe (WPI), The University of Tokyo Institutes for Advanced Study, The University of Tokyo, 5-1-5 Kashiwanoha, Kashiwa, Chiba 277-8583, Japan
[3] Center for Data-Driven Discovery, Kavli IPMU (WPI), UTIAS, The University of Tokyo, 5-1-5 Kashiwanoha, Kashiwa, Chiba 277-8583, Japan
[4] Center for Astrophysical Sciences, Department of Physics and Astronomy, Johns Hopkins University, 3400 N. Charles Street, Baltimore, MD 21218, USA
[5] Department of Physics, The University of Tokyo, 7-3-1 Hongo, Bunkyo, Tokyo 113-0033, Japan
[6] Kavli Institute for Astronomy and Astrophysics, Peking University, Beijing 100871, China
[7] Research Center for the Early Universe, Graduate School of Science, The University of Tokyo, 7-3-1 Hongo, Bunkyo-ku, Tokyo 113-0033, Japan
[8] Center for Frontier Science, Chiba University, 1-33 Yayoi-cho, Inage-ku, Chiba 263-8522, Japan
[9] Department of Astronomy, The University of Texas at Austin, 2515 Speedway Boulevard Stop C1400, Austin, TX 78712, USA
[10] Cosmic Dawn Center (DAWN), Niels Bohr Building, Radmandsgade 62–64, DK-2200 Copenhagen N, Denmark
[11] School of Physics and Technology, Wuhan University, Wuhan 430072, China
[12] Caltech/IPAC, 1200 E. California Blvd., Pasadena, CA 91125, USA
[13] European Southern Observatory, Karl-Schwarzschild-Str. 2, D-85748 Garching, Germany
[14] DTU Space, Technical University of Denmark, Building 327, Elektrovej, DK-2800 Kgs. Lyngby, Denmark
[15] Center for Computational Astrophysics, Flatiron Institute, 162 Fifth Avenue, New York, NY 10010, USA
[16] Kapteyn Astronomical Institute, University of Groningen, NL-9700 AV Groningen, The Netherlands
[17] Departamento de Fisica Teorica, Modulo 8, Facultad de Ciencias, Universidad Autonoma de Madrid, E-28049 Madrid, Spain
[18] CIAFF, Facultad de Ciencias, Universidad Autonoma de Madrid, E-28049 Madrid, Spain
[19] Department of Physics, University of Miami, 1320 Campo Sano Drive, Coral Gables, FL 33124, USA
[20] Department of Astronomy, School of Physics, Peking University, 209 Chengfu Road, Haidian District, Beijing 100871, China
[21] Technical University of Munich, TUM School of Natural Sciences, Department of Physics, James-Franck-Str. 1, D-85748 Garching, Germany
[22] Max-Planck-Institut fÃ¼r Astrophysik, Karl-Schwarzschild-Str. 1, D-85748 Garching, Germany
[23] NASA-Goddard Space Flight Center, Code 662, Greenbelt, MD 20771, USA
[24] Laboratory for Multiwavelength Astrophysics, School of Physics and Astronomy, Rochester Institute of Technology, 84 Lomb Memorial Drive, Rochester, NY 14623, USA
[25] Space Telescope Science Institute, 3700 San Martin Drive, Baltimore, MD 21218, USA
[26] Institut d'Astrophysique de Paris, UMR 7095, CNRS, and Sorbonne Université, 98 bis boulevard Arago, F-75014 Paris, France
[27] Jet Propulsion Laboratory, California Institute of Technology, 4800 Oak Grove Drive, Pasadena, CA 91001, USA
[28] Department of Astronomy and Astrophysics, University of California, Santa Cruz, 1156 High Street, Santa Cruz, CA 95064, USA
[29] Purple Mountain Observatory, Chinese Academy of Sciences, 10 Yuanhua Road, Nanjing 210023, China
[30] The Observatories of the Carnegie Institution for Science, 813 Santa Barbara St., Pasadena, CA 91101, USA
[31] Department of Computer Science, Aalto University, PO Box 15400, FI-00076 Espoo, Finland
[32] Department of Physics, Faculty of Science, University of Helsinki, FI-00014 Helsinki, Finland
[33] Institute for Physics, Laboratory for Galaxy Evolution and Spectral Modelling, Ecole Polytechnique Federale de Lausanne, Observatoire de Sauverny, Chemin Pegasi 51, CH-1290 Versoix, Switzerland

**Received:** 2024 August 22; **Accepted:** 2024 October 2

[34]INAF, Osservatorio Astronomico di Trieste, Via Tiepolo 11, I-34131 Trieste, Italy
[35]Instituto de AstrofÃ-sica de Canarias (IAC), E-38205 La Laguna, Spain
[36]Observatoire de Paris, LERMA, PSL University, 61 avenue de l'Observatoire, F-75014 Paris, France
[37]Université Paris-Cité, 5 rue Thomas Mann, F-75014 Paris, France
[38]Universidad de La Laguna, Avda. Astrofísico Fco. Sanchez, E-38205 La Laguna, Tenerife, Spain
[39]Center for Computational Astrophysics, Flatiron Institute, 162 5th Avenue, New York, NY 10010, USA
[40]Institute for Computational Cosmology, Department of Physics, Durham University, South Road, Durham DH1 3LE, UK
[41]Department of Physics and Astronomy, University of California, Riverside, 900 University Ave., Riverside, CA 92521, USA
[42]Niels Bohr Institute, University of Copenhagen, Jagtvej 128, DK-2200 Copenhagen N, Denmark
[43]School of Physics and Astronomy, Tel Aviv University, Tel Aviv 69978, Israel
[44]National Astronomical Observatory of Japan, 2-21-1 Osawa, Mitaka, Tokyo 181-8588, Japan
*E-mail: takumi.tanaka@ipmu.jp

## Abstract

The current paradigm for the co-evolution of galaxies and their supermassive black holes postulates that dust-obscured active galactic nuclei (AGNs) represent a transitional phase towards a more luminous and unobscured state. However, our understanding of dusty AGNs and their host galaxies at early cosmic times is inadequate due to observational limitations. Here, we present JWST observations of CID-931, an X-ray-detected AGN at a spectroscopic redshift of $z_{\rm spec} = 4.91$. Multiband NIRCam imaging from the COSMOS-Web program reveals an unresolved red core, similar to JWST-discovered dusty AGNs. Strikingly, the red core is surrounded by at least eight massive star-forming clumps spread over $1\farcs6 \approx 10$ kpc, each of which has a stellar mass of $10^9$–$10^{10}\,M_\odot$ and a radius of ∼0.1–1 kpc. The whole system amounts to $10^{11}\,M_\odot$ in stellar mass, higher than typical star-forming galaxies at the same epoch. In this system, gas inflows and/or complex merger events may trigger clump formation and AGN activity, thus leading to the rapid formation of a massive galaxy hosting a supermassive black hole. Future follow-up observations will provide new insights into the evolution of the galaxy–black hole relationship during such transitional phases in the early universe.

**Keywords:** galaxies: active — galaxies: evolution — galaxies: high-redshift



## 1 Introduction

The James Webb Space Telescope (JWST, Rigby et al. 2023) has opened explorations of the distant universe. JWST has discovered many massive galaxies with stellar masses of $M_* \sim 10^{11}\,M_\odot$ at $z \gtrsim 4$ (e.g., Chworowsky et al. 2023; de Graaff et al. 2024) and $M_* \sim 10^{10}\,M_\odot$ even at $z \gtrsim 10$ (Casey et al. 2024). Observational studies have also identified hundreds of quasars with high black hole masses ($M_{\rm BH} \gtrsim 10^8\,M_\odot$) at $z \gtrsim 5$ (e.g., Fan et al. 2023). However, the rapid growth mechanism(s) of galaxies and black holes in the early universe remains a key unresolved problem. The distant universe is likely to provide important insights into the observed relations between the properties of supermassive black holes (SMBHs) and galaxies such as stellar mass $M_*$, bulge mass $M_{\rm bulge}$, and stellar velocity dispersion $\sigma_*$ as seen at low $z$ (e.g., Magorrian et al. 1998; Kormendy & Ho 2013; Reines & Volonteri 2015).

In the galaxy and SMBH co-evolution paradigm (e.g., Hopkins et al. 2008), dusty active galactic nuclei (AGNs) are considered a transitional phase with AGN feedback expelling the dust to reveal an unobscured luminous quasar phase (e.g., Gilli et al. 2011; Vito et al. 2019; Kato et al. 2020; Fujimoto et al. 2022). Additionally, such feedback is considered to impact the interstellar medium (ISM), suppress star formation, and eventually lead to a massive quiescent galaxy.

Despite the importance of obscured AGNs in the lower-redshift universe, relatively less is known about high-$z$ obscured AGNs and their host galaxies. This gap results in missing pieces in our understanding of galaxy evolution in the early universe including the triggers of AGN activity and the processes driving the evolution of their host galaxies.

Recently, JWST has identified a new high-$z$ galaxy population named "little red dots" (LRDs), characterized by their compactness and red color at rest-frame optical wavelengths (e.g., Labbé et al. 2023a, 2023b; Furtak et al. 2023; Kocevski et al. 2023; Harikane et al. 2023; Akins et al. 2023, 2024; Barro et al. 2024; Matthee et al. 2024). In many cases, by definition, no extended components are detected even after point spread function (PSF) subtraction, thus truly showing a compact morphology that JWST cannot resolve ($\lesssim$200 pc).

The nature of LRDs is still debated: whether LRDs are dusty star-forming galaxies or dusty AGNs (e.g., Labbé et al. 2023b; Barro et al. 2024; Pérez-González et al. 2024; Ananna et al. 2024; Akins et al. 2024; Kokorev et al. 2024). JWST spectroscopic observations have confirmed broad emission lines [full width at half maximum (FWHM) >1000 km s$^{-1}$] in photometrically selected LRDs with high completeness (e.g., Greene et al. 2024 reported that 80% of objects with $m_{F277W} - m_{F444W} > 1.5$ have broad line features), suggesting that LRDs are dusty type-I AGNs (e.g., Harikane et al. 2023; Kokorev et al. 2023; Kocevski et al. 2023, 2024; Matthee et al. 2024; Furtak et al. 2024; Greene et al. 2024). Another notable feature is that the number density of LRDs (e.g., Kokorev et al. 2023; Kocevski et al. 2024; Akins et al. 2024) and high-$z$ AGNs (e.g., Onoue et al. 2023; Harikane et al. 2023; Maiolino et al. 2023; Scholtz et al. 2023) is higher than an extrapolation from the luminosity function based on the high-$z$ quasar studies prior to JWST (e.g., Matsuoka et al. 2018; Niida et al. 2020).

Of particular importance, constraining the stellar mass ($M_*$) of LRDs is challenging due to their compactness and difficulties in decomposing their spectral energy densities (SEDs). Upper limits on $M_*$ suggest $M_{\rm BH}/M_*$ ratios higher than the local mass relation, thus revealing overmassive black holes (e.g., Harikane et al. 2023; Kokorev et al. 2023; Killi et al. 2024; Furtak et al. 2024). The interpretation of such overmassive high-$z$ SMBHs in the co-evolution scheme—whether they represent the intrinsic SMBH population (e.g., Pacucci et al. 2023; Durodola et al. 2024) or a subset due to selection biases (e.g., Ding et al. 2023; Li et al. 2024)—continues to be debated. The compactness selection criteria used in previous

LRD studies may also bias the selected galaxies toward AGN-dominant systems lacking extended host-galaxy components.

To explore high-$z$ dusty AGNs free from the aforementioned possible biases, we search for LRD-like colored objects with extended host-galaxy components using COSMOS-Web, a JWST Cycle 1 large program (Casey et al. 2023). The morphology and structure of the underlying host galaxies may shed light on their formation, such as signs of mergers, interactions, or more secular processes. This paper reports the image-based analysis of an exceptional case, CID-931,[1] an X-ray-detected AGN at $z_{\rm spec} \sim 4.91$ with an unresolved red core and an extended highly clumpy structure at rest-frame optical wavelengths. The remainder of this paper is organized as follows. The data and the target are described in section 2. Section 3 introduces the image-based decomposition and SED fitting analysis. Then, we present the AGN- and galaxy-related results in section 4. Finally, we discuss how the nature of CID-931 relates to LRDs in the literature (section 5) and conclude with our results in section 6. Throughout this paper, the AB magnitude system (Oke & Gunn 1983) is adopted, and we assume a Chabrier (2003) initial mass function and a standard cosmology with $H_0 = 70\,{\rm km\,s^{-1}\,Mpc^{-1}}$, $\Omega_m = 0.30$, and $\Omega_\Lambda = 0.70$.

## 2 Data and target selection

### 2.1 Data

COSMOS-Web (PI: Jeyhan Kartaltepe and Caitlin Casey, GO1727, Casey et al. 2023 for the overview) is a JWST treasury survey program observed in Cycle 1 with wide-area coverage of 0.54 deg$^2$ using NIRCam (Rieke et al. 2023; *F115W*, *F150W*, *F277W*, *F444W*) and 0.19 deg$^2$ with MIRI (Bouchet et al. 2015; *F770W*). CID-931 is only covered by the four NIRCam filter images from COSMOS-Web. The data are reduced with the JWST Calibration Pipeline[2] version 1.10.0 and the calibration Reference Data System version 1075. The final pixel scale is $0\farcs030\,{\rm pixel^{-1}}$ (see M. Franco et al. in preparation for details of the image reduction).

In addition to the NIRCam images, we use data from Chandra/ACIS-I (COSMOS Chandra Merged Image Data Version 1.0, Civano et al. 2016[3]), Hubble Space Telescope HST/ACS (Koekemoer et al. 2007; *F814W*), Subaru Hyper Suprime-Cam (HSC Subaru Strategic Program DR3, Aihara et al. 2022; *grizy*), and Spitzer/IRAC and MIPS (S-COSMOS, Sanders et al. 2007; 3.6, 4.5, 5.6, 8.0, 24.0 $\mu$m). In this study, we also use the photometric information from the XMM–Newton COSMOS X-Ray Point Source Catalog (Cappelluti et al. 2009) and the Super-deblended catalog (Jin et al. 2018; Hershel/PACS 100, 160 $\mu$m, Hershel/SPIRE 250, 350, 500, 850 $\mu$m, and JCMT/SCUBA2 850 $\mu$m).

### 2.2 Identification of CID-931, an X-ray-detected AGN at $z = 4.91$

Previous LRD studies use color and morphological information to select high-$z$ AGN candidates from JWST imaging data (e.g., Labbé et al. 2023a, 2023b; Barro et al. 2024; Greene et al. 2024; Kocevski et al. 2024; Akins et al. 2024). Barro et al. (2024) employed a single color selection of $m_{F277W} - m_{F444W} > 1.5$ and found 37 LRDs. Greene et al. (2024) spectroscopically confirmed broad Balmer emission lines from such photometrically selected LRDs and suggested that a color selection of $m_{F277W} - m_{F444W} > 1.6$ can effectively select broad-line LRDs with a low contamination fraction. Kocevski et al. (2024) used a similar strategy, in which they performed continuum slope fitting to select LRDs over a wide redshift range.

To avoid a bias towards AGN-dominated systems, we apply a single color selection of $m_{F277W} - m_{F444W} > 1.5$ to the flux in each pixel separately [a pixel-by-pixel color selection; see T. S. Tanaka et al. (in preparation) for details of the selection method]. Our candidate list is then cross-matched to the COSMOS DEIMOS spectroscopic catalog (Hasinger et al. 2018), which includes 10718 objects using the Deep Imaging Multi-Object Spectrograph (DEIMOS, Faber et al. 2003) on the Keck II telescope. This results in the identification of CID-931 at RA (J2000.0) $= 10^{\rm h}01^{\rm m}26\farcs37$ and Dec (J2000.0) $= +02°04'25\farcs32$, which was targeted due to being an X-ray source. The DEIMOS spectrum provided the redshift $z_{\rm spec} = 4.911 \pm 0.005$ based on the $6.7\sigma$ detection of the Ly$\alpha$ line.

CID-931 was detected by Chandra and included in the COSMOS Legacy Survey Point Source Catalog (Civano et al. 2016) based on a 4.6 Ms Chandra X-ray observation on the COSMOS field, which strongly suggests the presence of an AGN. We note that Li et al. (2024) independently reported CID-931 as an offset AGN, in which AGNs and their host galaxies merge with non-active galaxies.

As shown in the top left panel of figure 1, CID-931 has a bright red core surrounded by a highly clumpy structure of various colors and extending up to ∼10 kpc ($1\farcs6$) in diameter. The DEIMOS slit covers almost all of the clumps (figure 2). While the individual clumps cannot be spatially resolved in the Subaru HSC images, CID-931 is observed as a single extended component with a Sérsic index of $n \sim 1$ and an effective radius of $r_{\rm e} \sim 0\farcs5$ (corresponding to ∼3 kpc) at wavelengths longer than the $i$ band. The whole system of CID-931 is undetected in the HSC $g$ and $r$ bands, consistent with its spectroscopic redshift of $z_{\rm spec} = 4.91$. Thus, we conclude that the clumpy structure is not a foreground object such as a star cluster in our Galaxy. These clumps show variety in their colors (see sub-subsection 4.4.1); therefore, they are unlikely to be gravitationally lensed multiple images.

CID-931 was not detected in Akins et al. (2024), which utilized compactness and $m_{F277W} - m_{F444W} > 1.5$ color selection and identified 447 LRDs from COSMOS-Web data. If we measure aperture photometry by centering on the red core, it can pass the compactness criteria with $F_{F444W,\,0\farcs2}/F_{F444W,\,0\farcs5} = 0.55$. However, the red core does not pass the color selection with $m_{F277W} - m_{F444W} = 1.1$ due to the contamination from a nearby clump. We note that the photometry of the red core alone, estimated from the image-based analysis (subsection 3.1), passes the color selection criteria (subsection 4.3).

## 3 Analysis

### 3.1 Image-based decomposition

Light from an unresolved AGN usually outshines the stellar emission from its host galaxy. Therefore, image-based decomposition methods are needed to extract information

[1] Dubbed "Crimson Behemoth" due to it showing a red core, possibly a dusty AGN, and being a massive galaxy with an unprecedented clumpy structure.

[2] H. Bushouse et al. 2023, JWST Calibration Pipeline, doi:10.5281/zenodo.7795697 ⟨https://github.com/spacetelescope/jwst⟩.

[3] ⟨https://irsa.ipac.caltech.edu/data/COSMOS/images/chandra/merged/⟩.

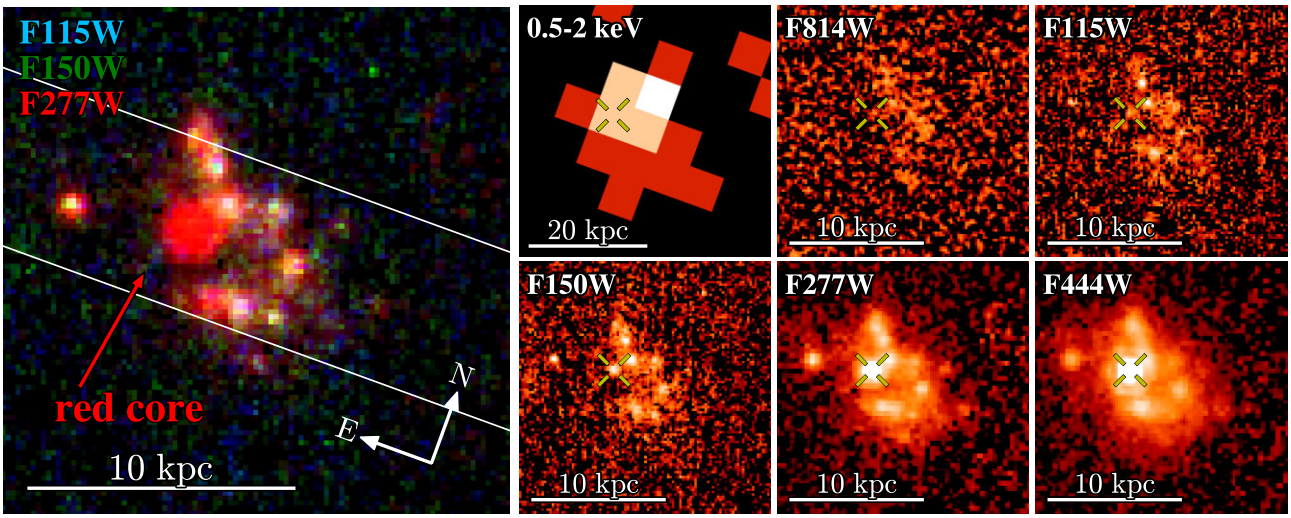


**Fig. 1.** Three-color (JWST/NIRCam *F277W*, *F150W*, and *F115W* for RGB) image and separate filter images of CID-931. The slit position of the Keck-II/DEIMOS observation is shown by the white lines. Note that the Chandra 0.5–2 keV image has a different cutout size (6″ × 6″) due to a much lower pixel scale (0.″984 pixel$^{-1}$) than the HST and JWST images (3″ × 3″ cutout with the pixel scale of 0.″03 pixel$^{-1}$). Yellow bars in right panels indicate the position of the red core..

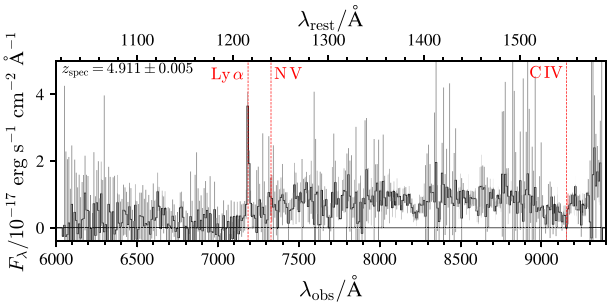


**Fig. 2.** Keck II/DEIMOS spectrum (Hasinger et al. 2018) binned over 20 spectral elements to increase the *S/N*. Gray lines indicate 1$\sigma$ error of each spectral bin. The positions of Ly$\alpha$, N V $\lambda$1240, and C IV $\lambda$1549 are indicated by vertical red lines.

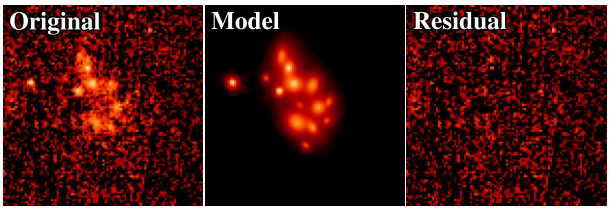


**Fig. 3.** Image-based decomposition analysis in the *F150W* filter: (left) original image of CID-931 (3″ × 3″), (middle) best-fitting model composed of a PSF component for the red core and Sérsic profiles for the other components, and (right) residual image, i.e., left minus right.

about the host galaxies (e.g., Ding et al. 2020, 2023; Zhuang et al. 2023; Tanaka et al. 2024; Kocevski et al. 2024). In this approach, the imaging data are fitted with a 2D model that combines a point spread function (PSF) component representing the AGN and a Sérsic profile(s) (Sérsic 1968), convolved with the PSF, representing the extended host galaxy. We can then remove the AGN emission by subtracting the PSF component from the original image.

To decompose the highly clumpy structure of CID-931 and obtain the flux of the red core component, we fit the imaging data from HST and JWST with a model composed of multiple components using the image analysis tool `galight` (Ding et al. 2020). First, we perform automatic segmentation on the *F150W* image, which offers a moderate signal-to-noise ratio *S/N* and spatial resolution compared to the other bands. We utilize the `detect_obj` function in `galight` to select regions with $S/N > 1.5$ that extend over more than 5 pixels. Then, we manually remove false detections from the automated segmentation map that are undetected in the other bands.

We finally separate the system into 13 components and the red core.

We use the position of each segmented component to construct a composite model. All components except the red core are fitted with single Sérsic profiles. For the red core, we attempt three different models: a PSF, a single Sérsic profile, and a PSF + a single Sérsic profile. Note that the red core and the other clumps are fitted simultaneously. We limit the effective radii $r_e$ and Sérsic indices $n$ to [0.″01, 0.″3] and [0.3, 9.0], respectively. The center position of each component is allowed to vary between different images within a range of 0.″1 around the initial estimates based on the *F150W* segmentation map.

Figure 3 presents our best model that reproduces the observed NIRCam images well. Comparing the fitting results using the three different models for the red core, the Bayesian information criterion (BIC) values indicate that $\rm BIC_{PSF}$ is less than $\rm BIC_{Sérsic} - 10$ and $\rm BIC_{PSF+Sérsic} - 10$ in all bands,[4] suggesting that the PSF component adequately describes the red core profile. Even using the Sérsic profile for the red core, the best-fitting $r_e$ is ∼0.″04 (∼0.3 kpc) in *F150W*, indicating a very compact morphology. Therefore, we derive the flux of the red core and the total system from the fitting results using the PSF component for the red core. The red core is not significantly detected in *F814W* ($S/N = 1.8$), and we use its 3$\sigma$ upper limit (= 0.030 $\mu$Jy) in the following SED analysis.

[4] For the thresholds for the BIC differences, we use 10, based on Kass and Raftery (1995).

**Table 1.** Major parameter settings in CIGALE SED fitting.

| Module | Parameter | Description | Values |
|---|---|---|---|
| `sfhdelayed` | `tau_main` | Timescale of delayed-$\tau$ SFH in Myr | 50, 100, 250, 500, 750, 1000, 2000 |
| | `age_main` | Starting time of delayed-$\tau$ SFH in Myr | 50, 100, 250, 500, 750, 1000 |
| `bc03` | `imf` | Initial mass function | 1: Chabrier (2003) |
| | `metallicity` | Stellar metallicity | 0.02 (solar metallicity) |
| `nebular` | `logU` | Ionization parameter | $-2$ |
| `dustatt_modified_starburst` | `E_BV_lines` | Color excess for the nebular lines | 0, 0.05, 0.1, 0.3, 0.5 |
| | `powerlaw_slope` | Slope delta of the power law modifying the attenuation curve | 0.0, 0.5, 1.0 |
| `skirtor2016` | `t` | AGN average edge-on optical depth at 9.7 $\mu$m | 3, 7, 11 |
| | `i` | Viewing angle in deg | 10, 30, 70 |
| | `delta` | Power-law index for modifying the disk SED | $-0.3$, 0, 0.3 |
| | `fracAGN` | AGN contribution to IR luminosity | 0.1, 0.2, 0.3, 0.4 |
| | `EBV` | Polar-dust color excess | 0, 0.05, 0.1, 0.3, 0.5, 0.75, 1.0 |

### 3.2 SED fitting analysis

We perform an SED fitting analysis for the whole system of CID-931 based on its total photometry from rest-frame X-ray to far-infrared wavelengths. For X-ray photometry, we utilize data from the Chandra Legacy Point Source Catalog (Civano et al. 2016). For HSC and Spitzer, we estimate the photometry after subtracting the contribution from a nearby star.

We use the total photometry obtained from 2D decomposition results (subsection 3.1) for HST and JWST. Because the Herschel and JCMT/SCUBA2 FIR photometry from the Super-deblended catalog (Jin et al. 2018) have $S/N \lesssim 2$, we use $3\sigma$ values as upper limits in the fitting.

We input these photometric data into CIGALE (Boquien et al. 2019; Yang et al. 2022) and fit them using a galaxy plus `skirtor2016` AGN template (Stalevski et al. 2012, 2016). For the stellar population model, we use the Bruzual and Charlot (2003) model (`bc03` module) and assume the initial mass function by Chabrier (2003). For the star-formation history, we assume a delayed-$\tau$ model that equalizes a star-formation rate (SFR) at each look-back time $t$ as

$$\mathrm{SFR}\,(t) \propto \begin{cases} (t - t_{\mathrm{age}}) \exp\left(-\dfrac{t - t_{\mathrm{age}}}{\tau}\right) & (t > t_{\mathrm{age}}), \\ 0 & (t < t_{\mathrm{age}}) \end{cases}, \qquad (1)$$

where $t_{\mathrm{age}}$ and $\tau$ are the starting time of star-formation activity and the SFR declining timescale. We also include nebular emission with the `nebular` module and fix the ionized parameter as $\log U = -2$. For dust attenuation, we utilize a `dustatt_modified_starburst` module that assumes the modified Calzetti et al. (2000) law. The detailed parameter settings are summarized in table 1.

We also implement a "pixel-by-pixel" SED fitting method, which performs SED fitting on photometry in each pixel using only HST and JWST imaging data. In this analysis, we first cut out the $3'' \times 3''$ region to cover all clumps around the red core.

We match the PSF sizes of the HST and JWST cutout images after subtracting the PSF component of the red core. For this procedure, we use *F444W* as a reference image, as its PSF is the largest among those of the images used. The images are binned by $2 \times 2$ pixel in order to increase the $S/N$ in each pixel, and the final pixel scale is $0\farcs060\,\mathrm{pixel}^{-1}$, which is still smaller than the PSF FWHM of *F444W* ($0\farcs14$–$0\farcs15$). Then, we only use the binned pixels with $S/N > 1$ in *F150W* in the fitting. Because we only use data of five rest-UV to rest-optical filters of HST and JWST, and the red core PSF component has been subtracted, the AGN component is not included in the SED fitting.

## 4 Results

As detailed below, CID-931 is an X-ray source confirmed to be at a spectroscopic redshift of $z_{\mathrm{spec}} = 4.91$ based on its rest-UV spectrum (subsection 4.1). The X-ray emission is luminous at this redshift, which can only be explained by an AGN (subsection 4.2). The red core shares a similar optical slope with known distant dusty AGNs and is likely responsible for the X-ray emission (subsection 4.3). Additionally, unlike other known high-$z$ dusty AGNs, the red core is uniquely surrounded by multiple massive star-forming clumps (subsection 4.4), which lends insight into its rapid assembly.

### 4.1 The rest-UV spectrum

The Keck II DEIMOS spectrum (figure 2) exhibits a Ly$\alpha$ emission line. From the single Gaussian + constant model fitting around Ly$\alpha$, we confirm that the Ly$\alpha$ line of CID-931 is a narrow line with the FWHM of $\sim$500 km s$^{-1}$. The Ly$\alpha$ obscured (not attenuation-corrected) line luminosity is $\sim 1.2 \times 10^{44}$ erg s$^{-1}$, which is around the bright end of the high-$z$ Ly$\alpha$ luminosity function (e.g., Konno et al. 2018; Goto et al. 2021; Morales et al. 2021).

Considering this line luminosity, the Ly$\alpha$ line contributes $\sim 0.4\,\mu$Jy to the *F814W* flux density, and it significantly exceeds the $3\sigma$ upper limit for the *F814W* flux density of the red core ($0.03\,\mu$Jy). Therefore, we consider that the Ly$\alpha$ line emission mainly comes from the star-forming clumps rather than the red core, which is the most likely AGN component of the CID-931 system. C IV $\lambda$1549, a typically observed highly ionized line in AGN spectra, is undetected. Significant dust attenuation in the red core can bury Ly$\alpha$ and C IV lines from the AGN.

### 4.2 X-ray emission

CID-931 is detected by Chandra in the soft band (0.5–2 keV) with $S/N = 4.4$ and full band (0.5–7 keV) with $S/N = 3.9$. However, CID-931 is not detected in the hard band (2–7 keV). CID-931 is also detected by XMM–Newton in the soft band (0.5–2 keV) with $S/N \sim 6$ and not detected in the hard band (2–10 keV).

The soft-band flux from XMM–Newton $(1.2 \pm 0.2) \times 10^{-15}\,\mathrm{erg\,s^{-1}\,cm^{-2}}$ is consistent with the flux from Chandra $(0.9 \pm 0.2) \times 10^{-15}\,\mathrm{erg\,s^{-1}\,cm^{-2}}$ within the $1\sigma$ uncertainty.

Because the X-ray net counts ($25.5 \pm 6.9$ counts) are insufficient for spectral analysis, it is challenging to strongly constrain parameters such as hydrogen column density $N_\mathrm{H}$ and photon index $\Gamma$. However, due to non-detection in the hard band, we assign an upper limit for the hard-band flux (90% confidence level estimated in Civano et al. 2016, $1.5 \times 10^{-15}\,\mathrm{erg\,cm^{-2}\,s^{-1}}$) and obtain an intrinsic $N_\mathrm{H}$ upper limit as $N_\mathrm{H} \lesssim 8 \times 10^{22}\,\mathrm{cm^{-2}}$, assuming a photon index $\Gamma = 1.9$ (e.g., Marchesi et al. 2016; Ricci et al. 2017). When using the XMM–Newton soft-band flux and the $3\sigma$ upper limit for the hard-band flux ($5 \times 10^{-15}\,\mathrm{erg\,cm^{-2}\,s^{-1}}$), we obtain an upper limit of $N_\mathrm{H}$ as $N_\mathrm{H} \lesssim 7 \times 10^{23}\,\mathrm{cm^{-2}}$. These upper limits are far from the threshold for being a Compton-thick AGN ($N_\mathrm{H} \gtrsim 10^{24}\,\mathrm{cm^{-2}}$). Therefore, we can rule out the possibility that CID-931 is a Compton-thick AGN.

Considering the intrinsic $N_\mathrm{H}$ range of $0 < N_\mathrm{H}/\mathrm{cm^{-2}} \lesssim 8 \times 10^{22}$ and accounting for the Galactic $N_\mathrm{H}$ (HI4PI Collaboration 2016, retrived from NASA HEASARC tools[5]), we obtain the X-ray unobscured luminosity of $2.6 \times 10^{44} < L_{[2-10\,\mathrm{keV}]}/\mathrm{erg\,s^{-1}} < 3.2 \times 10^{44}$. This X-ray unobscured luminosity cannot be attributed to only X-ray binaries; e.g., the relation between normal galaxy X-ray luminosity, $M_*$, and SFR (Lehmer et al. 2010) requires $M_* \sim 10^{16}\,M_\odot$ or $\mathrm{SFR} \sim 10^5\,M_\odot\,\mathrm{yr^{-1}}$ to describe the observed X-ray unobscured luminosity.

Therefore, the X-ray emission from CID-931 is securely due to an AGN.

### 4.3 The red core as a dusty AGN

With the red core well fitted by a PSF model and being the brightest component in CID-931, the simple interpretation is that the red core is the probable site of the X-ray source. However, the Chandra X-ray image (figure 1) lacks sufficient spatial resolution (size of 50% enriched energy fraction is about 2″–4″, Civano et al. 2016) to uniquely confirm which component in the CID-931 system corresponds to the X-ray source.

To assess the color of the red core, we fit the photometry from *F115W* to *F444W* by a single power-law SED model. We find that the spectral slope is $\beta = 2.08 \pm 0.13$, where $\beta$ is defined as $F_\lambda \propto \lambda^\beta$. The slope is significantly redder than that of a typical unobscured quasar ($\beta = -1.5$; e.g., Vanden Berk et al. 2001), and that of the whole system of CID-931 (figure 4).

The color index of the red core, $m_{F277W} - m_{F444W} = 1.5$ mag (2.1 mag when calculated from $\beta$), indicates that it is as red as high-$z$ dusty AGNs (e.g., Lambrides et al. 2024 reported $m_{F277W} - m_{F444W} = 1.8$ mag) and spectroscopically confirmed broad-line LRDs (e.g., Greene et al. 2024). Additionally, the *F277W* photometry shows a $2.8\sigma$ excess (−0.35 mag) over the fitted power law. This *F277W* excess potentially indicates contributions from Hβ + [O III] λλ4959, 5007 ($\lambda_\mathrm{obs} = 2.87, 2.93, 2.96\,\mu$m, respectively), similar to other spectroscopically confirmed JWST AGNs (Onoue et al. 2023; Kocevski et al. 2023; Solimano et al. 2024).

[5] ⟨https://heasarc.gsfc.nasa.gov/cgi-bin/Tools/w3nh/w3nh.pl⟩.

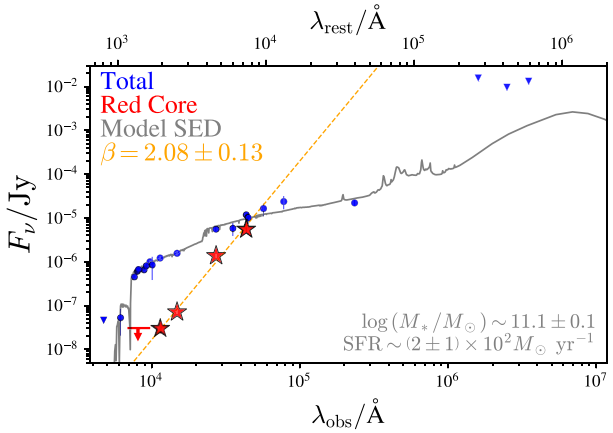


**Fig. 4.** SED of the full CID-931 system (blue) and the red core separately (red). Triangle markers indicate the $3\sigma$ upper limit. The orange line indicates the best-fitting power law of *F115W* to *F444W* photometry with $\beta = 2.08 \pm 0.13$. The gray line indicates the best-fitting model SED.

We also perform SED fitting for just the red core using the galaxy SED models without an AGN model. In this case, we recover a stellar mass of $10^{11.7}\,M_\odot$, which is much higher than typical $z = 5$ massive galaxies (e.g., Weaver et al. 2023). Moreover, the compact size of the red component yields a stellar mass density of $\Sigma_* \gtrsim 3 \times 10^{12}\,M_\odot\,\mathrm{kpc^{-2}}$. This is also significantly higher than the maximum $\Sigma_*$ ever found ($\Sigma_* \sim 3 \times 10^{11}\,M_\odot\,\mathrm{kpc^{-2}}$, Hopkins et al. 2010; Grudić et al. 2019). However, fitting with an AGN plus a galaxy composite model results in $\log(M_*/M_\odot) = 10.9 \pm 0.2$, accounting for ∼60% of the total $M_*$ (subsection 4.4). This analysis is supportive of the red core including a dusty AGN.

Assuming the SED of the red core to be entirely due to an AGN, we fit the HST and JWST photometry to determine the continuum spectral slope ($f_\lambda \propto \lambda^\beta$, e.g., Vanden Berk et al. 2001). We find $\beta = -1.5$ and then estimate the unobscured rest-2500 Å monochromatic luminosity $L_{2500}$ considering dust attenuation (Calzetti et al. 2000). This results in $A_V = 2.6 \pm 0.3$ mag, and $L_{2500} = 2.5^{+0.4}_{-0.3} \times 10^{32}\,\mathrm{erg\,s^{-1}\,cm^{-2}\,Hz^{-1}}$. As shown in figure 5, the value of $L_{2500}$ is similar to very UV-bright quasars (Lusso & Risaliti 2016; Nanni et al. 2017).

With the X-ray luminosity, we obtain $\alpha_\mathrm{OX} \sim -2.0$, which is the ratio of the X-ray (2 keV) monochromatic luminosity $L_\mathrm{2\,keV}$ to the rest-UV (2500 Å) monochromatic luminosity $L_{2500}$ defined as $\alpha_\mathrm{OX} = 0.384 \times \log(L_\mathrm{2\,keV}/L_{2500})$. Figure 5 indicates that the red core has an $\alpha_\mathrm{OX}$ value a little smaller than the relation by Lusso and Risaliti (2016).

Note that the above $L_{2500}$ estimation does not consider the contribution of the host-galaxy emission, which may lead to an overestimation of $L_{2500}$. Therefore, the estimated $L_{2500}$ should be treated as the upper limit. Figure 5 also shows the changes in $\alpha_\mathrm{OX}$ when $L_{2500}$ is lower than the estimated value, indicating that CID-931 would become closer to the relation by Lusso and Risaliti (2016) when $L_{2500}$ is overestimated. Accurately estimating the host-galaxy contribution with the currently available data is challenging, and it requires spectroscopic data of the red core that can be obtained through future IFU observations. We also need deeper X-ray observation to constrain $N_\mathrm{H}$ and decrease the uncertainty of $\alpha_\mathrm{OX}$.

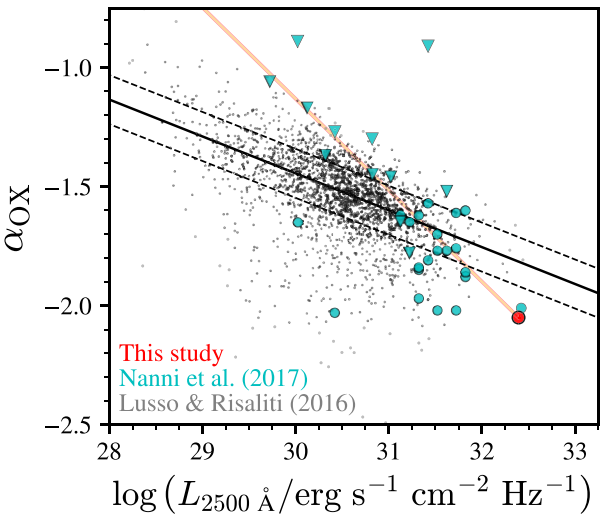


**Fig. 5.** Relation between $L_{2500}$ and $\alpha_{OX}$. Red, cyan, and gray circles indicate CID-931, high-$z$ ($z \sim 6$) luminous quasars in Nanni et al. (2017), and low-to-mid-$z$ (largely $z \lesssim 3$) AGNs in Lusso and Risaliti (2016). Black solid and dashed lines indicate the relation by Lusso and Risaliti (2016) and its $1\sigma$ interval. Triangle markers indicate the upper limit of $\alpha_{OX}$. An orange-shaded line indicates the potential change in $\alpha_{OX}$ depending on the decrease in $L_{2500}$ due to the uncertain host-galaxy contribution and dust extinction.

### 4.4 A massive clumpy star-forming host galaxy

Based on the SED fitting of the photometry of the entire complex with a galaxy + AGN template (subsection 3.2), we infer that the stellar mass of CID-931 is $\log(M_*/M_\odot) = 11.1 \pm 0.1$, and the total SFR is $(2 \pm 1) \times 10^2\ M_\odot\ \text{yr}^{-1}$. These results indicate that CID-931 is on the star-forming main sequence (SFMS) at $z \sim 5$ (e.g., Salmon et al. 2015; Khusanova et al. 2021). The stellar mass function by Weaver et al. (2023) predicts that only ∼1 galaxy with $\log(M_*/M_\odot) = 11.1 \pm 0.1$ is expected to fall within the COSMOS-Web coverage at $z \sim 4.5$–$5.5$. This result indicates that CID-931 lies within the most massive galaxy aggregation at $z \sim 5$, which is likely found thanks to the wide coverage of COSMOS-Web.

From pixel-by-pixel SED fitting results, we obtain the total stellar mass of $\log(M_*/M_\odot) = 10.7 \pm 0.2$ and total SFR of $(2.6 \pm 0.3) \times 10^2\ M_\odot\ \text{yr}^{-1}$. Since we remove and mask the red core region in the pixel-by-pixel SED fitting (subsection 3.2), the difference in the estimated values should arise from the red core part. Assuming this, the stellar mass difference of $\log(\Delta M_*/M_\odot) = 10.9 \pm 0.2$ would correspond to the stellar mass of the red core, which is consistent with the SED fitting results of only the red core ($\log(M_*/M_\odot) = 10.9 \pm 0.2$, subsection 4.3). There is a possibility that a spatially unresolved SED fitting is biased by the young stellar population (outshining problem, e.g., Maraston et al. 2010; Sorba & Sawicki 2018; Giménez-Arteaga et al. 2023, 2024; Narayanan et al. 2024), and directly comparing the results obtained from spatially unresolved and resolved methods might be problematic. Nevertheless, both methods consistently yield $M_* \sim 10^{11}\ M_\odot$ and SFR ∼ a few hundred $M_\odot\ \text{yr}^{-1}$, indicating that the CID-931 system is a massive star-forming galaxy (SFG) on the $z \sim 5$ SFMS.

#### 4.4.1 Individual clump properties

Clumpy structures are one of the important morphological features observed in high-$z$ star-forming galaxies (e.g., Elmegreen et al. 2009; Hainline et al. 2024; Kalita et al. 2024; Faisst et al. 2024; Harikane et al. 2024). Previous studies have demonstrated that clumpy structures represent rapid star formation triggered by violent disk instabilities (e.g., Dekel et al. 2009a, 2009b; Bournaud et al. 2011; Fujimoto et al. 2024) or merger-triggered growth (e.g., Jones et al. 2024; Nakazato et al. 2024; Harikane et al. 2024).

To discuss the characteristics of each clump, we focus on the most luminous eight components. Figure 6 shows the distribution of stellar mass density $\Sigma_*$ (panel a), SFR density $\Sigma_{SFR}$ (panel b), $A_V$ (panel c), the age of star-formation activity in the delayed-$\tau$ SFH, $t_{age}$ (panel d), and specific SFR (sSFR = SFR/$M_*$, panel e) for the eight clumps reconstructed from the pixel-by-pixel SED fitting results. Clumps have higher $\Sigma_*$ compared to regions without clumps, reaching up to $10^{10}\ M_\odot\ \text{kpc}^{-2}$. $\Sigma_{SFR}$ is also higher in the clumps, exceeding $10^{1.5}\ M_\odot\ \text{yr}^{-1}\ \text{kpc}^{-2}$. Additionally, the clumps tend to have smaller $t_{age}$ and larger sSFR. This tendency indicates that clumps contain recently formed stellar components within the CID-931 system. The $A_V$ map reveals that the clump in the southern part of CID-931, which has the highest $\Sigma_*$ and $\Sigma_{SFR}$, has a significant dust attenuation with $A_V > 2$, also consistent with the red color observed in the three-color image in figure 1.

Figure 7 presents the $UVJ$ diagram[6] and the relationships between size, SFR, and $M_*$ for each clump reconstructed from the 2D decomposition results. First, each pixel and clump is classified as an SFG in the $UVJ$ diagram (e.g., Williams et al. 2009). Each clump has a high stellar mass ($10^9 < M_* < 10^{10}\ M_\odot$), which is among the most massive clumps ever found (e.g., Elmegreen et al. 2009; Huertas-Company et al. 2020; Ambachew et al. 2022). The SFR–$M_*$ relation shows that each clump lies on the $z \sim 5$ SFMS, indicating that they are star-forming clumps.

Compared to the $z \sim 4$ size–mass relation of SFGs (Ward et al. 2024) based on JWST measurements, these clumps are approximately 10 times smaller in $r_e$ than $z \sim 4$ SFGs with similar $M_*$. The clumps exhibit $\Sigma_* \sim 10^{9-10}\ M_\odot\ \text{kpc}^{-2}$ consistent with or slightly higher than the extrapolation of the $z \sim 4$ size–mass relation of $UVJ$-selected quiescent galaxies (QGs, Ito et al. 2024). Since galaxy size is wavelength-dependent and the size–mass relations of Ward et al. (2024) and Ito et al. (2024) are based on $r_e$ at rest-frame 5000 Å, we use $r_e$ measurements in the *F277W* filter, which is the closest to the rest-frame 5000 Å at $z = 4.91$. However, the total $r_e$, indicated by the star in figures 7b and c, is based on HSC $i$-band measurements introduced in subsection 2.2. We do not correct for wavelength dependence for the total $r_e$ because CID-931 is not a single-galaxy system but a complex one that may not follow the typical size–wavelength relation. Even if we applied a correction using the size–wavelength relation from Ito et al. (2024), the total $r_e$ would change only from $r_e \sim 0\farcs5$ to ∼$0\farcs3$ without significantly altering its position on the $r_e$–$M_*$ or –SFR planes.

When compared to the spectroscopically confirmed $z > 5$ galaxies (Morishita et al. 2024), $M_*$ and SFR of our clumps are comparable with the most massive or highest-SFR galaxies and also show high values of $\Sigma_* \sim 10^{9-10}\ M_\odot\ \text{kpc}^{-2}$ and $\Sigma_{SFR} \sim 10^{1-2}\ M_\odot\ \text{yr}^{-1}\ \text{kpc}^{-2}$. These $\Sigma_*$ and $\Sigma_{SFR}$ are as high as those of gravitationally lensed clumps at $z \sim 6$ (Fujimoto et al. 2024; Giménez-Arteaga et al. 2024; Valentino et al.

[6] We calculated the model magnitude based on the best-fitting SED with the CIGALE SED fitting code. Due to the discrete model grid, the color indices are discrete, and some pixels have the same color indices in figure 7a.

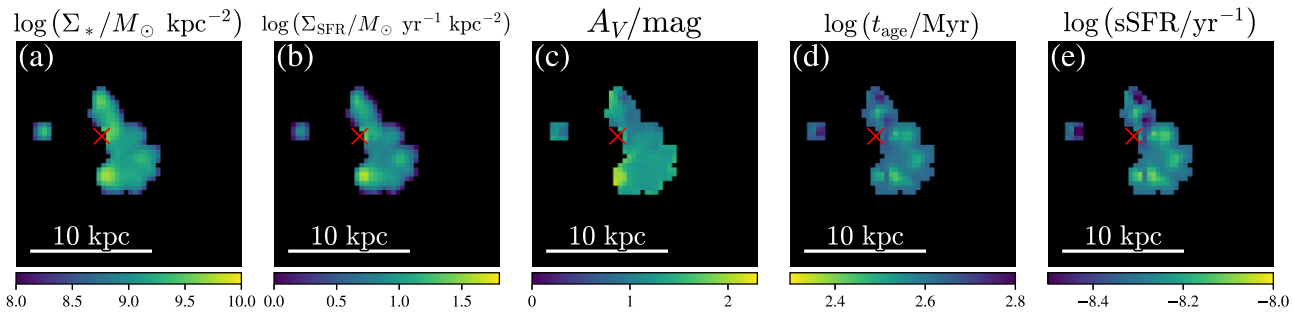


**Fig. 6.** Two-dimensional maps of each parameter from pixel-by-pixel SED fitting: (a) stellar mass density $\Sigma_*$, (b) SFR density $\Sigma_{\rm SFR}$, (c) $V$-band dust attenuation $A_V$, (d) starting time of star-formation activity in the delayed-$\tau$ SFH, $t_{\rm age}$, and (e) specific SFR. Note that the PSF component fitted to the red core is subtracted from the input imaging data, and the position of the red core is marked as a red cross. We see variations between clumps for each parameter.

2024). However, comparing the clumps in CID-931 and those reported in Fujimoto et al. (2024), there is a significant scale difference of approximately 10 times in $r_{\rm e}$, suggesting different types of objects.

Furthermore, Dessauges-Zavadsky et al. (2017) reported that observational limitations on spatial resolution lead to a lower limit of the detectable clump $M_*$. Also, the clumpy structures seen in Fujimoto et al. (2024) could not be resolved without gravitational lensing (see figure 2 in Fujimoto et al. 2024). Similarly, if the clumps in CID-931 are composed of clumps with smaller stellar masses with a separation smaller than spatial resolution, the absence of gravitational lens magnification would prevent us from resolving smaller clumps. If the observed clumps are the aggregation of smaller clumps, these smaller clumps should have a higher $\Sigma_{\rm SFR}$ and $\Sigma_*$ than the observed clumps. Assuming that each clump within the CID-931 system is further divided into smaller clumps with similar $M_*$ distribution ratios and $\Sigma_* \sim 10^{11}\,M_\odot\,{\rm kpc}^{-2}$, the smaller clumps would correspond to massive clusters, such as Galactic young massive clusters or nuclear star clusters (Norris et al. 2014), with masses of approximately $10^7$–$10^9\,M_\odot$ and sizes of $r_{\rm e} \sim 4$–$40$ pc. Such compact, dense clumps would be similar to the $z \gtrsim 6$ clumps previously observed thanks to gravitational lensing (e.g., Welch et al. 2023; Vanzella et al. 2023; Fudamoto et al. 2024; Fujimoto et al. 2024) and can be analogs of young massive star clusters (YMC, e.g., Portegies Zwart et al. 2010) in the local Universe, usually of pc-scale size.

### 4.5 Comparison with zoom-in simulations

Despite CID-931 having interesting features of a massive clumpy structure, the currently available observational data for CID-931 are limited.

In particular, the lack of high spatial resolution spectroscopic data from ALMA or JWST IFU prevents us from discussing the kinematics of each clump within the galaxy.

To discuss the possible formation mechanism of the observed clumpy structures, we use zoom-in cosmological simulations from FirstLight (Ceverino et al. 2017).

The simulation suite has a box size of 60 comoving Mpc, and the maximum spatial resolution is 17 pc, which is well suited to studying inner structures of massive rare galaxies such as CID-931. Note that our simulation does not include AGN feedback. In this section, we discuss the formation mechanism of massive clumpy galaxies at high redshift, assuming that the AGN feedback is negligible for the formation of clumpy morphologies.

Using the clumpy identification of Nakazato, Ceverino, and Yoshida (2024), we select clumpy galaxies with $M_* > 10^{10}\,M_\odot$ at a $z < 6$ snapshot and successfully find an analog of the clumpy galaxies with a stellar mass of $M_* = 10^{10.1}\,M_\odot$ at $z = 5.94$. Although the simulated analog is about 10 times less massive than CID-931, it is still considered a massive galaxy at $z \sim 6$, similar to CID-931. Thus, we regard it as an analog of a massive clumpy galaxy at high redshift.

Panels (a) and (b) of figure 8 show the surface density map of stellar mass ($\Sigma_*$) and SFR ($\Sigma_{\rm SFR}$). We see that clumps have $\Sigma_* \sim 10^{9-10}\,M_\odot\,{\rm kpc}^{-2}$ and $\Sigma_{\rm SFR} \sim 10^{1-2}\,M_\odot\,{\rm yr}^{-1}\,{\rm kpc}^{-2}$, which are consistent with those of CID-931 (figure 6). Dust attenuation of the simulated galaxies is calculated by using the post-processing radiative transfer code SKIRT (Baes et al. 2011; Camps & Baes 2020) in the same manner as in Behrens et al. (2018) and Y. Nakazato et al. (in preparation). Panel (c) of figure 8, showing the $V$-band attenuation map, indicates that the clumps have large $A_V$ values of $A_V \gtrsim 2$, similar to CID-931. Panels (d) and (e) of figure 8 exhibit the distribution of mass-weighted age and specific SFR (sSFR $\equiv \Sigma_{\rm SFR}/\Sigma_*$). The central core has an age of $\sim$120 Myr and sSFR of $\lesssim 1$ Gyr$^{-1}$, while the surrounding clumps are much younger ($\lesssim$50 Myr) and proceed via bursty star formation with sSFR $\gtrsim 10$ Gyr$^{-1}$.

We further generate the mock JWST three-color images as shown in the left panel of figure 9. The three filters of *F115W*, *F150W*, and *F277W* are combined and the corresponding PSF and transmission are considered. The mock image shows a red core and separated clump regions similar to CID-931. The three-color mock image also suggests that AGNs in complex clumpy systems may appear as offset AGNs (Li et al. 2024) with the other components separated when their clumps are significantly brighter than the disk and have asymmetric distributions.

Regarding the clump formation processes, we check the snapshots preceding the one shown in figure 9 and confirm that there are no merger events to trigger the clump formation. We also calculate the Toomre-$Q$ parameter (Toomre 1964), defined as

$$Q = \frac{\sigma\kappa}{AG\Sigma}, \tag{2}$$

where $\sigma$, $\kappa$, and $\Sigma$ are the radial velocity dispersion, the epicyclic frequency of a disk, and the surface density, respectively. $G$ and $A$ are the gravitational constant and numerical

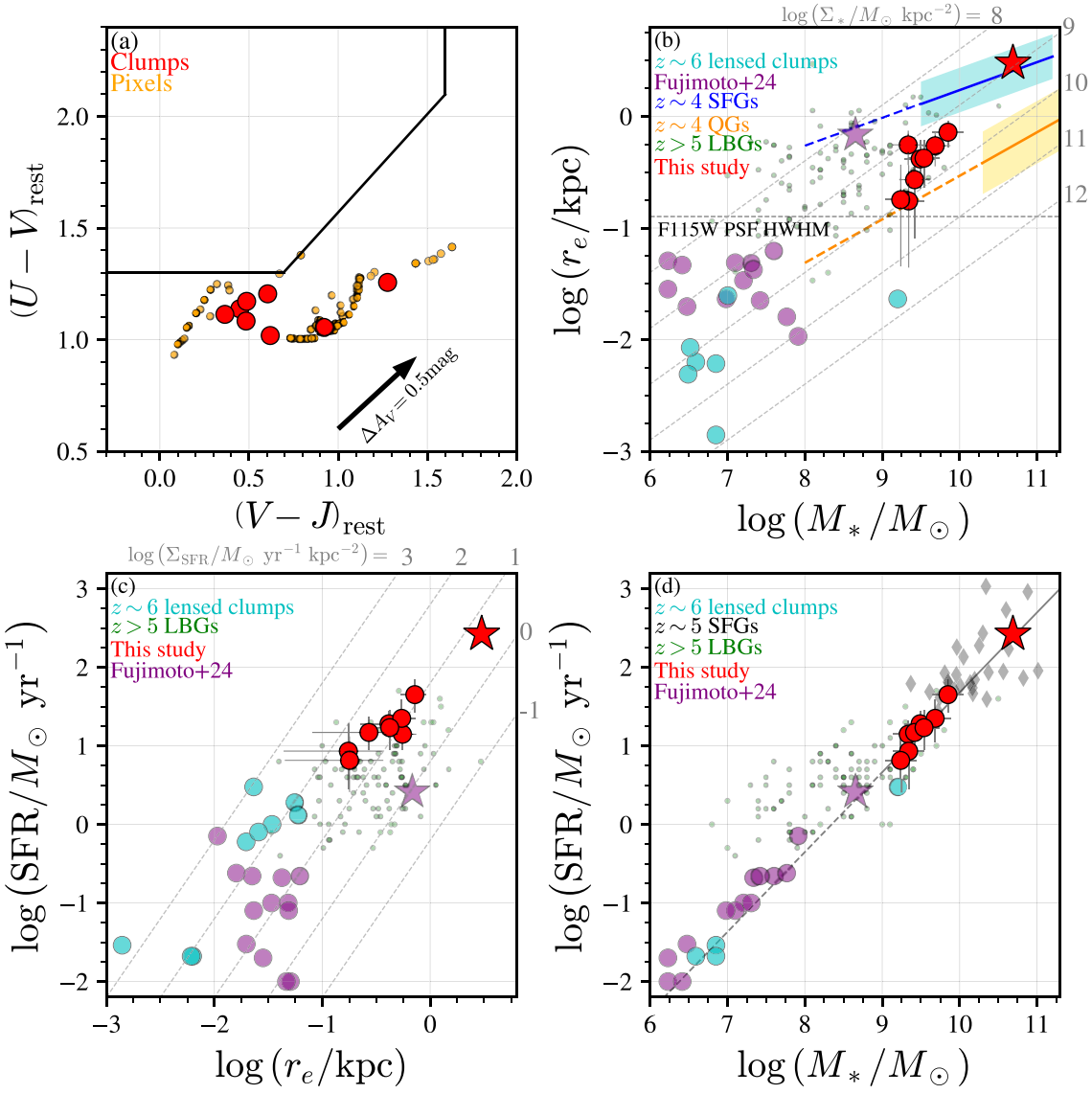


**Fig. 7.** Galaxy and clump characteristics. (a) Rest-frame *UVJ* color–color diagram. Orange and red dots indicate each pixel and clump, respectively. The black line indicates the threshold for classifying QGs and SFGs by Williams et al. (2009). The black arrow indicates the dust extinction corresponding to $\Delta A_V = 0.5$ mag. (b) Size ($r_e$)–mass ($M_*$) relation. Red and purple dots represent each clump in CID-931 and the $z\sim6$ clumpy system dubbed "Cosmic Grapes" in Fujimoto et al. (2024), respectively. Stars indicate the overall region of CID-931 and Cosmic Grapes (note that the red core component is not included in CID-931). Cyan dots indicate $z\gtrsim6$ lensed clumps (Welch et al. 2023; Vanzella et al. 2023; Fudamoto et al. 2024). Green dots represent high-$z$ Lyman break galaxies (LBGs, Morishita et al. 2024). The blue and orange lines and shaded regions indicate the size–mass relation for $z\sim4$ SFGs (Ward et al. 2024) and *UVJ*-selected QGs (Ito et al. 2024). The dashed lines indicate the extrapolation of each size–mass relation. The horizontal gray dashed line represents the half width at half maximum (HWHM) of the *F115W* PSF, while the diagonal gray dashed lines indicate fixed values of $\Sigma_*$. (c) Size ($r_e$)–SFR relation. Each marker is the same as in panel (b). The diagonal gray dotted lines indicate each $\Sigma_{\rm SFR}$. (d) SFR–$M_*$ relation. Each marker is the same as in panel (b). The gray diamonds indicate $z\sim5$ SFGs (Khusanova et al. 2021; Xiao et al. 2023). The black solid and dashed lines represent the $z\sim5$ SFMS (Khusanova et al. 2021) and its extrapolation. The total $M_*$ and SFR (red stars) are the sum of the values of each pixel. For the total $r_e$, we use $r_e$ for the HSC *i* band (subsection 2.2). Each clump in CID-931 is on the $z\sim5$ SFMS, massive with respect to the JWST SFG population, and more compact with higher $\Sigma_*$ and $\Sigma_{\rm SFR}$ than typical high-$z$ SFGs.

factor ($A=\pi$ for a gas disk and $A\simeq3.36$ for a stellar disk; see Toomre 1964; Elmegreen 2011; Inoue et al. 2016). When $Q\gg1$, the disk is in a stable state, and the effects of self-gravity are negligible.

Otherwise, $Q<1$ means that gravitational instability occurs with axisymmetric perturbation, leading to clump formation and disk fragmentation.

Note that Inoue et al. (2016) suggest that some protoclumps may show $Q>1$ and a low Toomre-$Q$ value does not fully trace clump formation through disk instability.

We calculate the Toomre-$Q$ map assuming a two-component disk of gas and stars (Ceverino et al. 2010; Romeo & Wiegert 2011; Romeo & Falstad 2013; Inoue et al. 2016) and present the face-on view in the right panel of figure 9. We see the apparent disk structure with $Q>1$ and clumps with $Q<1$, suggesting clump formation through violent disk instability. Therefore, the zoom-in simulation results suggest the possibility that violent disk instability can form massive clumpy structures in high-$z$ massive galaxies.

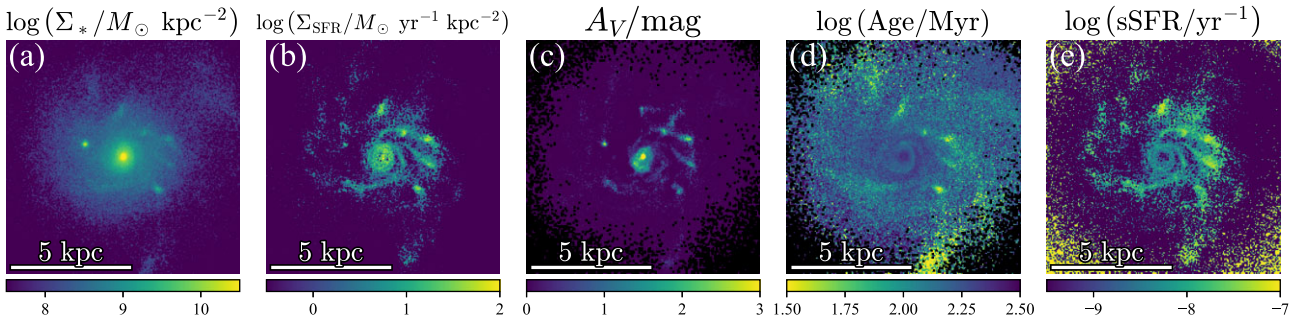


**Fig. 8.** Same for figure 6, but for the simulated galaxy.

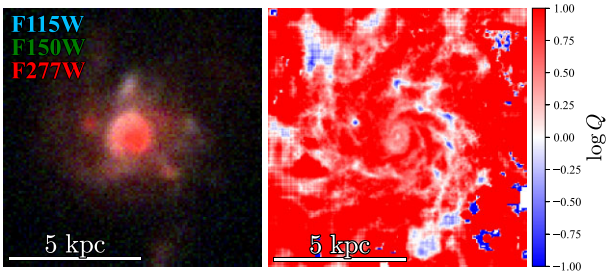


**Fig. 9.** (Left) Mock three-color (JWST/NIRCam *F277W*, *F150W*, and *F115W* for RGB) image of the simulated galaxy with $\log(M_*/M_\odot) \sim 10.1$ at $z \sim 5.94$. We convolve the image assuming a Gaussian PSF that corresponds to the physical size of the *F115W* PSF at $z \sim 4.91$. (Right) Toomre-$Q$ map. Blue and red indicate $Q < 1$ and $Q > 1$, respectively. The simulated galaxy similar to CID-931 suggests that the clumpy structure of these galaxies is formed through disk instability.

## 5 Discussion

### 5.1 Formation mechanism of the clumpy structure

The physical origins of these clumpy structures are essential to understanding the rapid galaxy formation and the relation with the AGN activity in the early Universe. However, it is still unclear which processes significantly contribute to clump formation, mergers or disk instabilities.

Explaining all clumps in CID-931 as merger-induced structures needs a highly complex merger event of multiple massive SFGs, at least eight galaxies with $M_* \sim 10^9$–$10^{10}\,M_\odot$. Jin et al. (2023) report such a complex merger event of massive galaxies, a $z \sim 5$ compact group of galaxies. The stellar mass range of each member galaxy is $M_* \sim 10^{8.4-9.8}\,M_\odot$, and Jin et al. (2023) discuss that the member galaxies will merge into a single massive ($M_* \sim 10^{11}$) galaxy at $z \sim 3$ based on the simulations. Compared with this compact group of galaxies, CID-931 is a little more compact than the object in Jin et al. (2023) (spread over $10 \times 20\,\mathrm{kpc}^2$) and may represent a stage where the member galaxies start accreting into the center and are about to merge. During such a period, the gas inflow into the central region caused by the interaction may trigger the AGN activity. This scenario is consistent with the galaxy–SMBH evolution paradigm by Hopkins et al. (2008).

The disk instability scenario suggests that star-forming clumps are formed through gravitational disk instability, possibly driven by gas inflow (e.g., Bournaud et al. 2011). It is worth noting that the $z \sim 6$ clumpy system in Fujimoto et al. (2024), which follows similar scaling relations to CID-931 (figure 7), is also suggested to be formed through disk instability from Toomre-$Q$ estimation based on ALMA observations. As described in subsection 4.5, zoom-in simulations find a galaxy with similar morphologies and clump properties to CID-931 and show that the clumps are formed by disk instabilities. In the disk instability scenario, the gas inflow may also supply dust and gas into the central region and initiate dusty AGN activity.

To identify the origin of the clumpy structure, we need to measure the kinematics of each clump and gas using spatially resolved spectroscopic data and evaluate disk instability by calculating Toomre-$Q$. Therefore, future high-spatial resolution and deep integral field spectroscopy with ALMA and JWST are necessary.

As discussed in sub-subsection 4.4.1, each clump might have multiple unresolved clumps that even JWST cannot spatially resolve. These components would be resolved using higher spatial resolution observations using ALMA or next-generation large telescopes, such as the next-generation Very Large Array (ngVLA), Extremely Large Telescope (ELT), and Thirty Meter Telescope (TMT).

### 5.2 SMBH–galaxy relation

Due to the lack of a near-infrared spectrum, we cannot measure the $M_{\rm BH}$ of the red core from the present photometric data.

Here, we estimate $M_{\rm BH}$ by assuming the Eddington limit, i.e., the maximum accretion speed. We convert the X-ray luminosity of CID-931 (subsection 4.2) to bolometric luminosity $L_{\rm bol} = (6.3 \pm 1.5) \times 10^{45}\,\mathrm{erg\,s^{-1}}$ by assuming a bolometric correction presented in Duras et al. (2020).

With the assumption of the Eddington limit accretion, the corresponding black hole mass is $M_{\rm BH} = (4.4 \pm 1.2) \times 10^7\,M_\odot$, which should be regarded as a lower limit. Note that the bolometric correction factor can be different for high-$z$ AGNs, as suggested in recent JWST studies (e.g., Maiolino et al. 2024; Juodžbalis et al. 2024).

The estimated $M_*$ and $M_{\rm BH}$ indicate a system with higher $M_*$ than those found by JWST among LRDs and high-$z$ AGNs (figure 10). Meanwhile, J2236+0032, a low-luminosity quasar at $z = 6.40$ reported in Ding et al. (2023), has similar masses of $\log(M_*/M_\odot) = 11.12^{+0.40}_{-0.27}$ and $M_{\rm BH} = (15.4 \pm 2.7) \times 10^8 M_\odot$. Also note that some high-$z$ quasars are estimated at similar dynamical masses $M_{\rm dyn} \sim 10^{11}\,M_\odot$ (e.g., Izumi et al. 2019, 2021; Neeleman et al. 2021).

In the widely accepted BH–galaxy evolution paradigm (e.g., Hopkins et al. 2008), dusty AGNs are in a transitional phase evolving into unobscured quasars by expelling dust. Therefore, CID-931 potentially evolves into the high-$z$ quasars

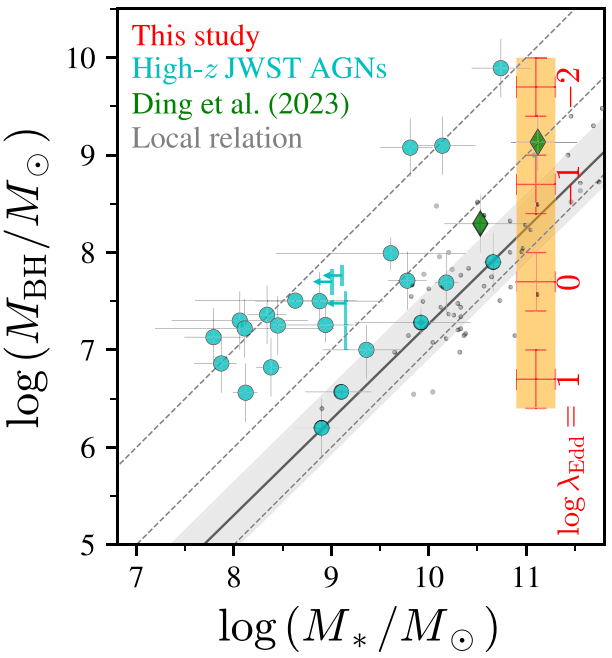


**Fig. 10.** Relation between $M_{\rm BH}$ and $M_*$. Cyan, green, and gray plots indicate the high-$z$ JWST-discovered AGNs (Harikane et al. 2023; Maiolino et al. 2023; Yue et al. 2023), $z \sim 6$ low-luminosity quasars (Ding et al. 2023), and the local active (Bennert et al. 2011) and inactive galaxies (Häring & Rix 2004). The orange rectangle shows the possible positions of CID-931 with different Eddington ratio values $\lambda_{\rm Edd}$. Gray dashed and black solid lines indicate the mass ratio values $\log(M_{\rm BH}/M_*) = -3, -2, -1$ and the local mass relation obtained from the fitting of the samples in Häring and Rix (2004) and Bennert et al. (2011).

reported in previous studies with $M_*$ or $M_{\rm dyn} \sim 10^{11}\,M_\odot$. Additionally, simulation studies have suggested that high-$z$ giant and high-$\Sigma_*$ clumps accumulate at the center to form a bulge (e.g., Elmegreen et al. 2008; Ceverino et al. 2010, 2012; Bournaud et al. 2014; Mandelker et al. 2014, 2017).

CID-931 may also evolve into a massive elliptical galaxy as its clumps coalesce to form a bulge. We can verify this scenario through spectroscopic follow-up observations by exploring outflows to discuss AGN feedback and constraining SFR and depletion time to discuss future mass growth.

The clumpy structure of CID-931 suggests that its AGN activity is associated with active star formation or a complex merger event (subsection 5.1). DeGraf et al. (2017) also suggested that such clumps accrete into the central region and contribute to the strong outflow by fueling the AGN. Following this scenario, future accretion of the currently observed massive clumps in CID-931 may trigger AGN feedback to expel the dust, leading to evolution into an unobscured quasar. Systematic studies of dusty AGN host galaxies are required to deepen our understanding of the relationship between AGN activity and host-galaxy evolution in the transitioning phase.

### 5.3 Comparisons with JWST's LRDs

LRD studies (e.g., Greene et al. 2024) have reported very red colors and a V-shaped SED characterized by a change in the spectral slope around $\lambda_{\rm rest} \sim 3000$–$4000$ Å. In the case of CID-931, the slope observed in *F115W* and *F150W* ($\lambda_{\rm rest} \sim 2000$–$2500$ Å) is similar to the slope in *F277W* and *F444W* (rest-frame $\lambda_{\rm rest} \sim 4700$–$7500$ Å). Due to the lack of V-shaped SED for the red core, we do not conclude that CID-931 is the same type of object as existing LRDs. However, given the uniqueness of CID-931 as a high-$z$ X-ray-detected dusty AGN with a similar spectral slope in the rest-optical to LRDs, it is still worth comparing CID-931 with existing LRDs in the literature to better understand the nature of both CID-931 and LRDs.

Most of the previously found LRDs are undetected in X-ray (Kocevski et al. 2023; Furtak et al. 2023; Matthee et al. 2024) even after a stacking analysis (Yue et al. 2024; Ananna et al. 2024; Maiolino et al. 2024; Akins et al. 2024), except for only two cases among hundreds of LRDs reported as X-ray detected (Kocevski et al. 2024).

Interestingly, the two X-ray-detected LRDs in Kocevski et al. (2024) have a massive ($M_* \sim 10^{10.6}\,M_\odot$) stellar component (PRIMER-COS 3866 with $L_{\rm bol} \sim 1 \times 10^{46}\,{\rm erg\,s^{-1}}$ at $z_{\rm spec} = 4.66$) or an extended blue clumpy structure (JADES 21925 with $L_{\rm bol} \sim 1 \times 10^{45}\,{\rm erg\,s^{-1}}$ at $z_{\rm photo} = 3.1$).[7] In subsection 4.2, we also find that CID-931 has an $N_{\rm H}$ upper limit of $N_{\rm H} \lesssim 8 \times 10^{22}\,{\rm cm^{-2}}$ and is not a Compton-thick AGN ($N_{\rm H} \gtrsim 10^{24}\,{\rm cm^{-2}}$). This $N_{\rm H}$ upper limit is also consistent with both of the two X-ray-detected LRDs from Kocevski et al. (2024) with $N_{\rm H} \sim 10^{23}\,{\rm cm^{-2}}$. Therefore, compared to typical X-ray-undetected LRDs that usually lack host-galaxy components, high-$z$ X-ray-detected LRDs or dusty AGNs (Kocevski et al. 2024 and this study) might represent a different population with extended host-galaxy components.

For further and solid discussion, it is crucial to enlarge the sample of similar X-ray- or host-detected high-$z$ dusty AGNs to perform a statistical abundance comparison and make spectroscopic observations to compare with typical LRDs. Future deeper X-ray telescopes such as Athena should enlarge the sample size of high-$z$ X-ray-detected AGNs.

## 6 Conclusions

Applying the pixel-by-pixel color selection method on the JWST high spatial-resolution imaging data obtained with the COSMOS-Web program, we discover a red unresolved component surrounded by a clumpy structure in CID-931, an X-ray-detected AGN at $z_{\rm spec} = 4.91$. CID-931 is a unique high-$z$ system with X-ray detection as solid evidence of an AGN and a very complex clumpy morphology, which we can directly detect without complicated imaging decomposition analysis.

We conduct a detailed analysis of CID-931 based on the JWST imaging data.

Image-based decomposition indicates that the red core, the brightest component in the *F277W* and *F444W* images, shows a rest-optical color similar to those of high-$z$ dusty AGNs and LRDs (figure 4), suggesting that it is a dusty AGN.

Analysis of the X-ray flux shows that the AGN in CID-931 is not a Compton-thick AGN ($N_{\rm H} \lesssim 8 \times 10^{22}\,{\rm cm^{-2}}$ corresponding to the limiting depth in the Chandra observation), similar to the X-ray-detected LRDs reported by Kocevski et al. (2024). We also find that the red core has a large bolometric luminosity of $L_{\rm bol} \sim 6.3 \times 10^{45}\,{\rm erg\,s^{-1}}$.

SED fitting reveals that the entire CID-931 is a massive system with $M_* \sim 10^{11}\,M_\odot$, similar to the mass observed in high-$z$ quasars (e.g., Izumi et al. 2019; Ding et al. 2023). We roughly estimate the $M_{\rm BH}$ from the bolometric luminosity and find that CID-931 has a significantly larger stellar mass than existing

[7] The bolometric luminosity values are calculated from the bolometric correction by Duras et al. (2020).

JWST-found AGNs and occupies a different parameter space on the $M_{BH}$–$M_*$ plane (figure 10).

CID-931 has at least eight massive star-forming clumps over $1.''6 \approx 10$ kpc. Although each clump has a high $M_*$ ($\sim 10^{9-10}\,M_\odot$) and SFR ($\sim 10^{1-2}\,M_\odot\,\mathrm{yr}^{-1}$) comparable with high-$z$ Lyman break galaxies, they have much more compact morphology, suggesting higher $\Sigma_*$ ($\sim 10^{9-10}\,M_\odot\,\mathrm{kpc}^{-2}$) and $\Sigma_{SFR}$ ($\sim 10^{1-2}\,M_\odot\,\mathrm{yr}^{-1}\,\mathrm{kpc}^{-2}$) as shown in figure 7.

We discussed two possible formation mechanisms for the CID-931 clumpy structure. One scenario is that the massive clumps are massive galaxies that are accreting and coalescing into a single massive galaxy. The other scenario is that gas inflows cause clump formation through violent disk instability, as suggested by zoom-in simulations (figure 9). Such a merger event or gas inflow might also have triggered the AGN activity by supplying gas into the central region.

We propose the possibility that the X-ray-detected LRDs, all of which have host-galaxy components, represent a different population from previously discovered LRDs. Also, considering that typical LRDs usually lack an X-ray detection and a host-galaxy component, X-ray-detected and host-detected LRDs might bridge between typical LRDs and existing SMBH + galaxy systems.

To discuss the role of such objects in the galaxy–SMBH evolution more solidly, it is essential to increase the sample of X-ray-detected or host-galaxy-detected high-$z$ AGNs, discuss their statistical properties, and perform abundance comparisons. For this purpose, utilizing spatial information is useful because it can select host-detected dusty AGNs that are overlooked in typical selection methods (see T. S. Tanaka et al. in preparation).

For a more detailed evaluation of SMBH activity, including spectroscopic identification of the AGN, measurement of $M_{BH}$, and exploration of AGN outflows to study AGN feedback, spatially resolved and deep rest-optical follow-up observation with JWST/NIRSpec IFU is needed. Future high spatial and velocity resolution observations by ALMA could measure the kinematics of each clump within the host galaxy, enabling the calculation of the Toomre-$Q$ parameter to assess whether the host galaxy accumulates mass through mergers or disk instability.

Additionally, future ultra-high spatial resolution observations using ngVLA, ELT, and TMT are needed to spatially resolve finer clump structures that even JWST cannot. Also, deeper X-ray observations are needed to strongly constrain $N_H$ and $\Gamma$, possibly with future deeper X-ray telescope surveys, such as Athena.

## Acknowledgments

We thank Kei Ito, Makoto Ando, and Suin Matsui for the fruitful discussion. We thank the anonymous referee for helpful feedback. This work is based on observations made with the NASA/ESA/CSA James Webb Space Telescope. The data were obtained from the Mikulski Archive for Space Telescopes at the Space Telescope Science Institute, which is operated by the Association of Universities for Research in Astronomy, Inc., under NASA contract NAS 5-03127 for JWST. These observations are associated with program IDs 1727 and 1837. Numerical computations were in part carried out on the iDark cluster, Kavli IPMU and the analysis servers at Center for Computational Astrophysics, National Astronomical Observatory of Japan. This work was made possible by utilizing the CANDIDE cluster at the Institut d'Astrophysique de Paris, which was funded through grants from the PNCG, CNES, DIM-ACAV, and the Cosmic Dawn Center and maintained by Stephane Rouberol.

## Funding

Kavli IPMU is supported by the World Premier International Research Center Initiative (WPI), MEXT, Japan. TT is supported by the Forefront Physics and Mathematics Program to Drive Transformation (FoPM), a World-leading Innovative Graduate Study (WINGS) Program at the University of Tokyo. YN acknowledges funding from JSPS KAKENHI Grant Number 23KJ0728 and a JSR fellowship. YF acknowledge support by JSPS KAKENHI Grant Numbers JP22K21349 and JP23K13149. SJ is supported by the European Union's Horizon Europe research and innovation program under the Marie Skłodowska-Curie grant No. 101060888.

## References

Aihara, H., et al. 2022, PASJ, 74, 247
Akins, H. B., et al. 2023, ApJ, 956, 61
Akins, H. B., et al. 2024, arXiv:2406.10341
Ambachew, L., et al. 2022, MNRAS, 512, 3079
Ananna, T. T., Bogdán, Á., Kovács, O. E., Natarajan, P., & Hickox, R. C. 2024, ApJ, 969, L18
Baes, M., Verstappen, J., De Looze, I., Fritz, J., Saftly, W., Vidal Pérez, E., Stalevski, M., & Valcke, S. 2011, ApJS, 196, 22
Barro, G., et al. 2024, ApJ, 963, 128
Behrens, C., Pallottini, A., Ferrara, A., Gallerani, S., & Vallini, L. 2018, MNRAS, 477, 552
Bennert, V. N., Auger, M. W., Treu, T., Woo, J.-H., & Malkan, M. A. 2011, ApJ, 726, 59
Boquien, M., Burgarella, D., Roehlly, Y., Buat, V., Ciesla, L., Corre, D., Inoue, A. K., & Salas, H. 2019, A&A, 622, A103
Bouchet, P., et al. 2015, PASP, 127, 612
Bournaud, F., et al. 2014, ApJ, 780, 57
Bournaud, F., Dekel, A., Teyssier, R., Cacciato, M., Daddi, E., Juneau, S., & Shankar, F. 2011, ApJ, 741, L33
Bruzual, G., & Charlot, S. 2003, MNRAS, 344, 1000
Calzetti, D., Armus, L., Bohlin, R. C., Kinney, A. L., Koornneef, J., & Storchi-Bergmann, T. 2000, ApJ, 533, 682
Camps, P., & Baes, M. 2020, Astron. Comput., 31, 100381
Cappelluti, N., et al. 2009, A&A, 497, 635
Casey, C. M., et al. 2023, ApJ, 954, 31
Casey, C. M., et al. 2024, ApJ, 965, 98
Ceverino, D., Dekel, A., & Bournaud, F. 2010, MNRAS, 404, 2151
Ceverino, D., Dekel, A., Mandelker, N., Bournaud, F., Burkert, A., Genzel, R., & Primack, J. 2012, MNRAS, 420, 3490
Ceverino, D., Glover, S. C. O., & Klessen, R. S. 2017, MNRAS, 470, 2791
Chabrier, G. 2003, PASP, 115, 763
Chworowsky, K., et al. 2024, AJ, 168, 113
Civano, F., et al. 2016, ApJ, 819, 62
de Graaff, A., et al. 2024, arXiv:2404.05683
DeGraf, C., Dekel, A., Gabor, J., & Bournaud, F. 2017, MNRAS, 466, 1462
Dekel, A., et al. 2009a, Nature, 457, 451
Dekel, A., Sari, R., & Ceverino, D. 2009b, ApJ, 703, 785
Dessauges-Zavadsky, M., Schaerer, D., Cava, A., Mayer, L., & Tamburello, V. 2017, ApJ, 836, L22
Ding, X., et al. 2020, ApJ, 888, 37
Ding, X., et al. 2023, Nature, 621, 51
Duras, F., et al. 2020, A&A, 636, A73
Durodola, E., Pacucci, F., & Hickox, R. C. 2024, arXiv:2406.10329

Elmegreen, B. G. 2011, ApJ, 737, 10
Elmegreen, B. G., Bournaud, F., & Elmegreen, D. M. 2008, ApJ, 688, 67
Elmegreen, D. M., Elmegreen, B. G., Marcus, M. T., Shahinyan, K., Yau, A., & Petersen, M. 2009, ApJ, 701, 306
Faber, S. M., et al. 2003, Proc. SPIE, 4841, 1657
Faisst, A. L., et al. 2024, arXiv:2405.09619
Fan, X., Bañados, E., & Simcoe, R. A. 2023, ARA&A, 61, 373
Fudamoto, Y., et al. 2024, ApJ, 961, 71
Fujimoto, S., et al. 2022, Nature, 604, 261
Fujimoto, S., et al. 2024, arXiv:2402.18543
Furtak, L. J., et al. 2023, ApJ, 952, 142
Furtak, L. J., et al. 2024, Nature, 628, 57
Gilli, R., et al. 2011, ApJ, 730, L28
Giménez-Arteaga, C., et al. 2023, ApJ, 948, 126
Giménez-Arteaga, C., et al. 2024, A&A, 686, A63
Goto, H., et al. 2021, ApJ, 923, 229
Greene, J. E., et al. 2024, ApJ, 964, 39
Grudić, M. Y., Hopkins, P. F., Quataert, E., & Murray, N. 2019, MNRAS, 483, 5548
Hainline, K., et al. 2024, ApJ, 964, 71
Harikane, Y., et al. 2023, ApJ, 959, 39
Harikane, Y., et al. 2024, arXiv:2406.18352
Häring, N., & Rix, H.-W. 2004, ApJ, 604, L89
Hasinger, G., et al. 2018, ApJ, 858, 77
HI4PI Collaboration 2016, A&A, 594, A116
Hopkins, P. F., Hernquist, L., Cox, T. J., & Kereš, D. 2008, ApJS, 175, 356
Hopkins, P. F., Murray, N., Quataert, E., & Thompson, T. A. 2010, MNRAS, 401, L19
Huertas-Company, M., et al. 2020, MNRAS, 499, 814
Inoue, S., Dekel, A., Mandelker, N., Ceverino, D., Bournaud, F., & Primack, J. 2016, MNRAS, 456, 2052
Ito, K., et al. 2024, ApJ, 964, 192
Izumi, T., et al. 2019, PASJ, 71, 111
Izumi, T., et al. 2021, ApJ, 914, 36
Jin, S., et al. 2018, ApJ, 864, 56
Jin, S., et al. 2023, A&A, 670, L11
Jones, G. C., et al. 2024, A&A, 682, A122
Juodžbalis, I., et al. 2024, MNRAS, 535, 853
Kalita, B. S., Silverman, J. D., Daddi, E., Mercier, W., Ho, L. C., & Ding, X. 2024, arXiv:2402.02679
Kass, R. E., & Raftery, A. E. 1995, J. Am. Statistical Assoc., 90, 773
Kato, N., et al. 2020, PASJ, 72, 84
Khusanova, Y., et al. 2021, A&A, 649, A152
Killi, M., et al. 2024, A&A, 691, A52
Kocevski, D. D., et al. 2023, ApJ, 946, L14
Kocevski, D. D., et al. 2024, arXiv:2404.03576
Koekemoer, A. M., et al. 2007, ApJS, 172, 196
Kokorev, V., et al. 2023, ApJ, 957, L7
Kokorev, V., et al. 2024, ApJ, 975, 178
Konno, A., et al. 2018, PASJ, 70, S16
Kormendy, J., & Ho, L. C. 2013, ARA&A, 51, 511
Labbé, I., et al. 2023a, Nature, 616, 266
Labbe, I., et al. 2023b, arXiv:2306.07320
Lambrides, E., et al. 2024, ApJ, 961, L25
Lehmer, B. D., Alexander, D. M., Bauer, F. E., Brandt, W. N., Goulding, A. D., Jenkins, L. P., Ptak, A., & Roberts, T. P. 2010, ApJ, 724, 559
Li, J., et al. 2024, MNRAS, 527, 4690
Lusso, E., & Risaliti, G. 2016, ApJ, 819, 154
Magorrian, J., et al. 1998, AJ, 115, 2285
Maiolino, R., et al. 2023, arXiv:2308.01230
Maiolino, R., et al. 2024, arXiv:2405.00504
Mandelker, N., Dekel, A., Ceverino, D., DeGraf, C., Guo, Y., & Primack, J. 2017, MNRAS, 464, 635
Mandelker, N., Dekel, A., Ceverino, D., Tweed, D., Moody, C. E., & Primack, J. 2014, MNRAS, 443, 3675
Maraston, C., Pforr, J., Renzini, A., Daddi, E., Dickinson, M., Cimatti, A., & Tonini, C. 2010, MNRAS, 407, 830
Marchesi, S., et al. 2016, ApJ, 830, 100
Matsuoka, Y., et al. 2018, ApJ, 869, 150
Matthee, J., et al. 2024, ApJ, 963, 129
Morales, A. M., Mason, C. A., Bruton, S., Gronke, M., Haardt, F., & Scarlata, C. 2021, ApJ, 919, 120
Morishita, T., et al. 2024, ApJ, 963, 9
Nakazato, Y., Ceverino, D., & Yoshida, N. 2024, ApJ, 975, 238
Nanni, R., Vignali, C., Gilli, R., Moretti, A., & Brandt, W. N. 2017, A&A, 603, A128
Narayanan, D., et al. 2024, ApJ, 961, 73
Neeleman, M., et al. 2021, ApJ, 911, 141
Niida, M., et al. 2020, ApJ, 904, 89
Norris, M. A., et al. 2014, MNRAS, 443, 1151
Oke, J. B., & Gunn, J. E. 1983, ApJ, 266, 713
Onoue, M., et al. 2023, ApJ, 942, L17
Pacucci, F., Nguyen, B., Carniani, S., Maiolino, R., & Fan, X. 2023, ApJ, 957, L3
Pérez-González, P. G., et al. 2024, ApJ, 968, 4
Portegies Zwart, S. F., McMillan, S. L. W., & Gieles, M. 2010, ARA&A, 48, 431
Reines, A. E., & Volonteri, M. 2015, ApJ, 813, 82
Ricci, C., et al. 2017, ApJS, 233, 17
Rieke, M. J., et al. 2023, PASP, 135, 028001
Rigby, J., et al. 2023, PASP, 135, 048001
Romeo, A. B., & Falstad, N. 2013, MNRAS, 433, 1389
Romeo, A. B., & Wiegert, J. 2011, MNRAS, 416, 1191
Salmon, B., et al. 2015, ApJ, 799, 183
Sanders, D. B., et al. 2007, ApJS, 172, 86
Scholtz, J., et al. 2023, arXiv:2311.18731
Solimano, M., et al. 2024, arXiv:2407.13020
Sorba, R., & Sawicki, M. 2018, MNRAS, 476, 1532
Stalevski, M., Fritz, J., Baes, M., Nakos, T., & Popović, L. Č. 2012, MNRAS, 420, 2756
Stalevski, M., Ricci, C., Ueda, Y., Lira, P., Fritz, J., & Baes, M. 2016, MNRAS, 458, 2288
Sérsic, J. L. 1968, Atlas de Galaxias Australes (Cordoba: Observatorio Astronomico)
Tanaka, T. S., et al. 2024, arXiv:2401.13742
Toomre, A. 1964, ApJ, 139, 1217
Valentino, F., et al. 2024, A&A, 685, A138
Vanden Berk, D. E., et al. 2001, AJ, 122, 549
Vanzella, E., et al. 2023, ApJ, 945, 53
Vito, F., et al. 2019, A&A, 628, L6
Ward, E., et al. 2024, ApJ, 962, 176
Weaver, J. R., et al. 2023, A&A, 677, A184
Welch, B., et al. 2023, ApJ, 943, 2
Williams, R. J., Quadri, R. F., Franx, M., van Dokkum, P., & Labbé, I. 2009, ApJ, 691, 1879
Xiao, M.-Y., et al. 2023, A&A, 672, A18
Yang, G., et al. 2022, ApJ, 927, 192
Yue, M., et al. 2024, ApJ, 966, 176
Yue, M., Eilers, A.-C., Ananna, T. T., Panagiotou, C., Kara, E., & Miyaji, T. 2024, ApJ, 974, L26
Zhuang, M.-Y., Li, J., & Shen, Y. 2024, ApJ, 962, 93

Received: 2024 August 22; Accepted: 2024 October 2